
Article:
Harris, B., Krös, L., C Nave, A. S. et al. (2 more authors) (2023) The spatial density distribution of H2O2 in the effluent of the COST-Jet and the kINPen-sci operated with a humidified helium feed gas. Plasma Sources Science and Technology. 115010. ISSN: 0963-0252

https://doi.org/10.1088/1361-6595/ad0742

PAPER • **OPEN ACCESS**

The spatial density distribution of H_2O_2 in the effluent of the COST-Jet and the kINPen-sci operated with a humidified helium feed gas

To cite this article: B Harris *et al* 2023 *Plasma Sources Sci. Technol.* **32** 115010

OPEN ACCESS
IOP Publishing
Plasma Sources Science and Technology
Plasma Sources Sci. Technol. **32** (2023) 115010 (13pp)
https://doi.org/10.1088/1361-6595/ad0742

The spatial density distribution of H_2O_2 in the effluent of the COST-Jet and the kINPen-sci operated with a humidified helium feed gas

B Harris[1,3,*], **L Krös**[2,3,*], **A S C Nave**[2], **E Wagenaars**[1] **and J H van Helden**[2]

[1] York Plasma Institute, School of Physics, Engineering and Technology, University of York, Heslington, York YO10 5DD, United Kingdom
[2] Leibniz Institute for Plasma Sci. Technol. (INP), Felix-Hausdorff-Str. 2, 17489 Greifswald, Germany

E-mail: benjamin.harris@york.ac.uk and levin.kroes@inp-greifswald.de

Received 30 June 2023, revised 15 September 2023
Accepted for publication 26 October 2023
Published 13 November 2023

Abstract

Cold atmospheric plasma jets operated with a helium feed gas containing small admixtures of water vapour are excellent sources of H_2O_2 for direct biomedical applications. However, H_2O_2 is typically distributed non-uniformly throughout the effluent region, meaning the dosage received by a patient or substrate is dependent on their positioning relative to the plasma source. This study presents the spatial distribution of absolute H_2O_2 number densities in the effluent of two popular plasma jets, the COST-Jet and the kINPen-sci plasma jet, when operated with a humidified helium feed gas. The measurements were performed using continuous wave cavity ring-down spectroscopy with a tunable, mid-infrared laser. The H_2O_2 number density measured close to the jet nozzle is 2.3×10^{14} cm^{-3} for the kINPen-sci plasma jet and 1.4×10^{14} cm^{-3} for the COST-Jet. The average number density of H_2O_2 in the effluent of the kINPen-sci plasma jet is a factor of two higher than in the effluent of the COST-Jet. The distribution of H_2O_2 in the COST-Jet effluent is initially highly uniform and suggests negligible mixing of H_2O_2 with the ambient air up to 15 mm from the jet nozzle, although it is rapidly diluted at further distances. In the case of the kINPen-sci plasma jet, the number density of H_2O_2 has a more pronounced radial distribution close to the nozzle, while the mixing with the ambient air is more gradual at further distances from the nozzle. It is evident that a detailed understanding of the H_2O_2 production in the plasma source, as well as of the transport of H_2O_2 to the substrate through the effluent, is required in order to optimise the intended effects. This work serves to highlight the difference of the distinct spatial distribution of H_2O_2 in the effluent of both types of plasma jets when considering their direct application in biomedicine.

Keywords: cold atmospheric plasma jet, cavity ring-down spectroscopy, humidified helium, hydrogen peroxide

[3] These authors contributed equally.
[*] Authors to whom any correspondence should be addressed.

1. Introduction

Cold atmospheric plasma jets (CAPJs) have generated much interest over the last decade. Their versatility has allowed their application in medicine, materials processing, green industry and agriculture [1–7]. When operated with a helium feed gas containing small admixtures of water vapour, CAPJs can generate reactive oxygen and nitrogen species (RONS) in appreciable quantities [8–10]. The effluent region of CAPJs contains a complex mixture of these RONS, making these devices desirable for biomedical applications such as microbial sterilisation, cancer therapy, and the treatment of chronic wounds [11–13]. The spatial distribution in the effluent varies for different RONS, influenced by a given species' mass and available reaction pathways. Hence, the dosage and mixture of RONS received through direct CAPJ treatment is dependent on the position of the substrate relative to the jet nozzle. It is therefore crucial to know how key RONS are spatially distributed throughout the effluent in order to understand their production mechanisms, as well as to be able to tailor the amount of each RONS depending on the application. However, spatially resolved density measurements of species in the plasma effluent pose a challenge for conventional diagnostics. While absorption spectroscopic techniques are excellent for measuring absolute number densities, the millimetre-scale geometries yield a short optical absorption path and are therefore hampered by a poor signal-to-noise ratio [14]. Multi-pass cells may be employed to increase the absorption path length through the gas mixture of the effluent, but the increased signal comes at the cost of any spatial resolution [15, 16]. To achieve both good sensitivity and spatial resolution, more complex experimental methods must be utilised. One such option is the use of cavity-enhanced spectroscopy techniques, in which an optical cavity composed of two highly reflective mirrors, positioned around the sample, is typically utilised. Coupling a laser beam into the cavity allows the beam to pass through the sample repeatedly to substantially increase its optical path length while maintaining high spatial resolution [17]. Cavity-enhanced spectroscopy techniques offer detection sensitivities with upper limits in the parts-per-trillion range at atmospheric pressure [18].

Cavity ring-down spectroscopy (CRDS) is an established technique for the analysis of atmospheric pressure plasma jets, starting with the measurement of OH in microwave plasma jets [19–22]. Zaplotnik *et al* demonstrated its use for radio-frequency plasmas by characterising the density of the $He(2^3S_1)$ metastable along the radial and symmetry axes in the effluent of a pulsed-power pure helium CAPJ [23]. Likewise, Benedikt *et al* presented radial and axial density distributions of the OH radical in the effluent of a humidified helium plasma generated with a COST-Jet-like plasma source [24]. Gianella *et al* employed optical feedback cavity-enhanced absorption spectroscopy to measure the HO_2 radical in the effluent of the kINPen-sci plasma jet supplied with a humidified argon feed gas [25] and later used their experimental measurements applying continuous wave CRDS (cw-CRDS) to develop and benchmark a HO_2 reaction kinetics model [26]. However, those measurements only yield line-of-sight integrated information. As a next step, Klose *et al* applied an Abel inversion to the obtained line-of-sight integrated densities, allowing the full spatial density distributions of HO_2 and H_2O_2 to be measured throughout the effluent of a kINPen-sci plasma jet supplied with a humidified argon feed gas [27, 28]. Other diagnostic techniques are also capable of probing the plasma effluent with good sensitivity and spatial resolution. Laser-induced fluorescence (LIF) was used by Verreycken *et al* to measure the density distribution of OH along the effluent of the kINPen09 in humidified argon [29], while Yatom *et al* employed the technique to obtain the time evolution of atomic hydrogen in the effluent of a nanosecond-pulsed, humidified argon CAPJ [30]. Klose *et al* also measured the spatial distributions of atomic oxygen and hydrogen in the effluent of the kINPen-sci plasma jet in humidified argon with picosecond two-photon absorption LIF (ps-TALIF) [5]. Consequently, there is now a plethora of data available on the spatial distributions of different RONS and their precursors in humidified argon plasmas [27, 28, 31, 32].

Spatially resolved measurements of humidified helium plasmas have also been obtained. In addition to Benedikt *et al*'s aforementioned study of OH for a COST-Jet-like plasma source [24], Schröter *et al* applied ps-TALIF to the COST Reference Microplasma Jet to investigate the influence of feed gas humidity on radical chemistry [33]. ps-TALIF was also employed by Myers *et al*, who presented the spatial density distribution of atomic oxygen in the effluent of the COST Reference Microplasma Jet for pure helium, humidified helium, and $He+O_2$ gas mixtures [34]. The relative spatial distribution of OH in the effluent of the COST Reference Microplasma Jet was obtained by Stapelmann *et al* using LIF, in an investigation mapping the transport of radicals from the effluent, through a liquid and to a model biological target [35]. Recently, van den Bekerom *et al* also used LIF to obtain the two-dimensional spatial distribution of OH and H_2O_2 mole fractions in a nanosecond-pulsed dielectric barrier discharge [36]. The absolute number density of H_2O_2 in humidified helium mixtures was measured by Willems *et al*, who used molecular beam mass spectrometry to obtain the H_2O_2 density distribution along the effluent of a COST-Jet-like plasma source [37]. Other gas mixtures have been investigated in a similar manner, including an investigation by Preissing *et al* that used LIF to measure the density of NO in the effluent of the COST Reference Microplasma Jet for $He/N_2/O_2$ mixtures [38]. Overall, full spatial distributions of species in the effluent of CAPJs remain relatively scarce for humidified helium plasmas. The distribution of a species is expected to vary between CAPJ designs as a result of the different types of discharge due to, for example, different electrode arrangement and methods of power coupling. Hence, this influences which CAPJ design is best suited for a given application. In this study, therefore, the absolute number density of H_2O_2 in the effluent of two widely-used CAPJs operated with humidified helium as a feed gas was investigated. The first plasma source is a CAPJ designed to match the specifications of the COST Reference Microplasma Jet (abbreviated to COST-Jet

in this work) [39]. The COST-Jet was created to act as a reference standard between research groups, but has also seen much applied use [40]. The second CAPJ of interest is the kINPen plasma jet, the first device of its kind to be CE-certified and made commercially available for medical use [31, 41]. The scientific version built purely for research, the kINPen-sci plasma jet, was used in this work [31, 42]. Using the experimental setup described by Klose *et al* [28], cw-CRDS is used to obtain the spatial density distribution of H_2O_2 in the effluent of both CAPJs.

2. Experimental setup

2.1. Plasma sources: COST-Jet and kINPen-sci plasma jet

A schematic of the COST-Jet and the kINPen-sci plasma jet is shown in figure 1. A full specification for the COST-Jet is presented in [39]. To summarise, the COST-Jet is a capacitively-coupled non-thermal plasma source, featuring two coplanar electrodes with a length of 30 mm and a thickness of 1 mm. A continuous voltage waveform with a radio frequency of 13.56 MHz and peak-to-peak voltage of 850 V is supplied to the powered electrode by a radio-frequency signal generator (RFG 150-13, Coaxial Power Systems), while the other electrode is grounded. The electrodes are separated by a 1 mm gap through which the feed gas flows, forming a plasma channel when power is supplied. The electrodes and channel are sealed within a quartz housing with a gap for the plasma effluent. The dimensions of the plasma channel are 30 mm $\times$ 1 mm $\times$ 1 mm. While the source is designed to match the electrode assembly laid out in the original COST-Jet schematic, it lacks an internal tuning capacitor and is instead impedance matched via an external L-network unit (MMN 150-13, Coaxial Power Systems).

A detailed review and specification of the kINPen-sci plasma jet is given in [31]. The kINPen-sci plasma jet is a dielectric barrier discharge-like (DBD-like) non-thermal plasma source and consists of a powered pin-type electrode inside a dielectric capillary, with the end of this capillary surrounded by a grounded electrode ring. The feed gas is introduced via the capillary, which has an inner diameter of 1.6 mm. The kINPen-sci plasma jet includes a standard purpose-built power supply, in this case supplying the electrode pin with a continuous voltage waveform with a peak-to-peak voltage of 3 kV and frequency of 860 kHz.

Both CAPJs are operated with humidified helium containing the same admixture of water vapour to the feed gas. The mixture is achieved by passing helium at a flow rate of 0.2 standard litre per minute (slm) through a bubbler containing deionised water (volume: 500 ml, temperature: 296 K), which is then combined with dry helium flowing at 0.8 slm. The CAPJs are thus operated with a total feed gas flow of 1 slm humidified helium. The feed gas humidity is measured with a hygrometer (DewMaster, Edgetech) to contain (3300 $\pm$ 100) ppm H_2O by volume.

The symmetry axis of the plasma effluent is defined as the z-axis. For both CAPJs, this position is normalised to the tip of the respective jet's nozzle, such that the effluent exits the source at $z = 0$. There is no visible photon emission in the effluent of the COST-Jet, while photon emission is seen to extend up to $z = 7.5$ mm for the kINPen-sci plasma jet. The effluent is allowed to protrude freely into open air, rather than being directed at a surface.

2.2. cw-CRDS

Measurements of H_2O_2 were performed using cw-CRDS, using the experimental setup described by Klose *et al* [28]. A schematic of the cw-CRDS setup used to measure line-of-sight-integrated densities of H_2O_2 is shown in figure 2. The optical cavity is composed of two highly reflective mirrors (Lohnstar Optics, reflectivity 99.98%, radius of curvature 100 cm), separated by a distance of 54.5 cm and mounted within mirror holders on a rail. The first cavity mirror holder is connected to a piezoelectric ring actuator (RA12-24, Piezosystem Jena) and a function generator (AFG 3000 C, Tektronix), so that the cavity length is continuously modulated by 4 μm. The cavity is partially covered by two metal tubes and purged with nitrogen gas flowing at 1 slm to minimise the influence of airborne pollutants, such as particulate matter (e.g. dust) and other absorbing species, notably water. The metal tubes are each 20 cm long and 5 cm in diameter. The inner ends of the tubes are left open, forming an outlet for the purging gas. The large outlet surface area relative to the nitrogen flow rate ensures that the efflux of nitrogen does not disturb the plasma effluent.

A quantum cascade laser (QCL) with a tuning range of 1224–1234 cm^{-1} (HHL-223, Alpes Lasers) was used, allowing optical transitions in the ν_6 band of H_2O_2 to be probed [28, 43–45]. The laser control unit comprised a low-noise QCL driver (QCL1000, Wavelength Electronics) and temperature controller (PTC5K-CH, Wavelength Electronics). A multifunctional data acquisition card (USB-6341 X Series, National Instruments) controlled the laser power and frequency by setting the values of the supplied current and temperature. The laser beam was split into two diffraction orders by guiding it through an acousto-optic modulator (AOM) (1208-G80-4, Isomet), with the zeroth diffraction order guided to a wavemeter (Laser Spectrum Analyser 771 B, Bristol Instruments) to monitor the laser frequency during operation. The AOM coupled 85% of the laser power into the first diffraction order, which was in turn coupled into the optical cavity through a system of gold-coated mirrors and mode matching lenses, in order to match the beam shape of the laser to the cavity modes. An off-axis parabolic mirror focused the laser beam exiting the cavity onto a fast detector (PVI-4TE-8-1x1, Vigo Systems, 790 MHz high cut-off frequency), with the signal recorded by an oscilloscope (Waverunner Xi-A, Teledyne LeCroy, band width: 400 MHz, sample rate: 5 GS s^{-1}) connected to a personal computer (PC). The intracavity power was allowed to increase until the detector signal reached a previously set

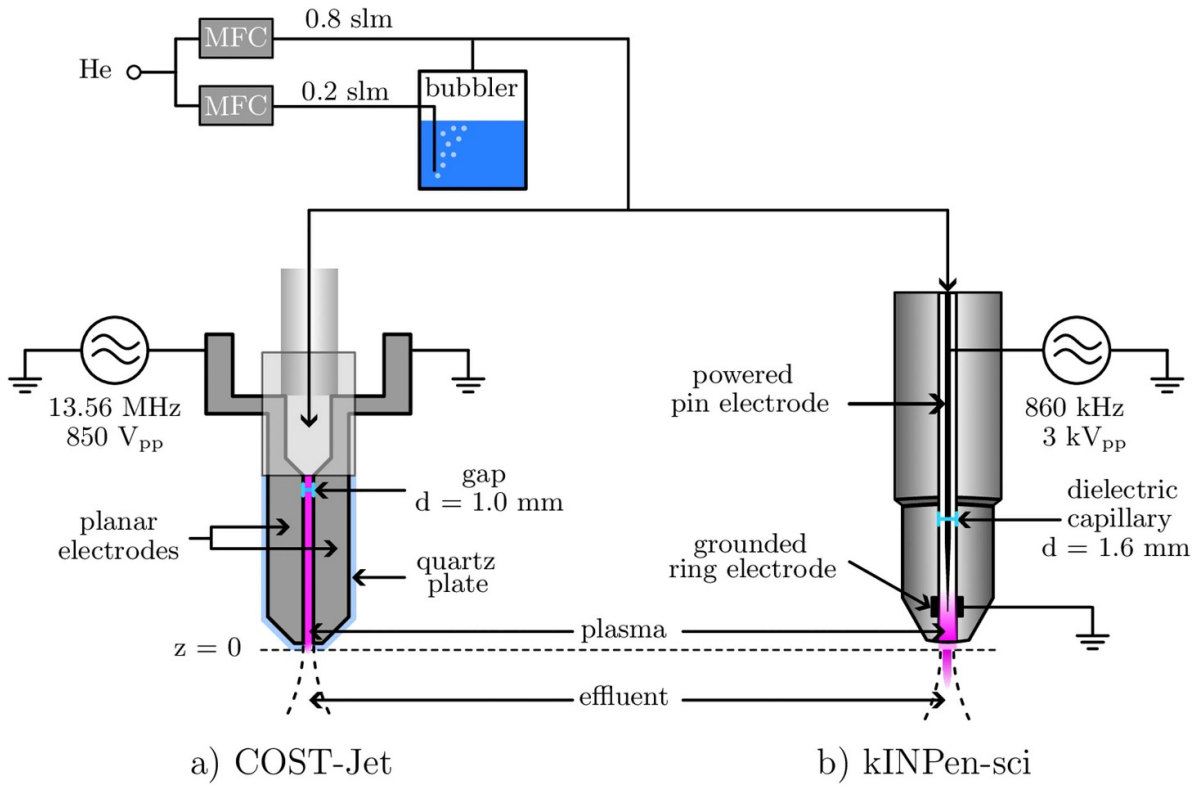

Figure 1. Schematic of (a) the COST-Jet and (b) the kINPen-sci plasma jet. MFC: mass flow controller.

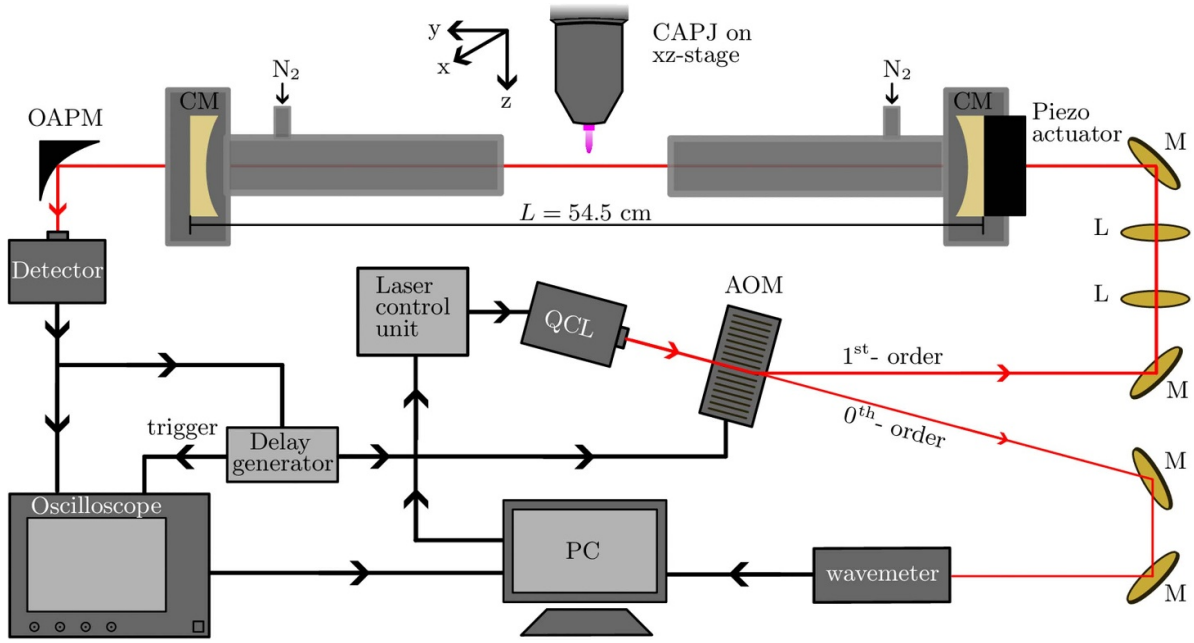

Figure 2. Schematic of the cw-CRDS setup used to study the density of H_2O_2 in the effluent of CAPJs. QCL: quantum cascade laser, AOM: acousto-optic modulator, M: gold-coated mirror, L: mode matching lens, CM: cavity mirror, OAPM: off-axis parabolic mirror.

threshold of typically 1 V. Once this occurred, a delay generator (DG535, Stanford Research Systems) temporarily cut the radio-frequency supply of the AOM, which stopped the first diffraction order of the beam from reaching the cavity and caused the intensity in the cavity to decay exponentially. From this, the ring-down time τ, defined as the time taken for the laser intensity inside the cavity to decay to $(1/e)$ of its initial intensity, was determined. Varying the laser frequency, referred to in terms of the equivalent wavenumber ν, allowed a cavity loss spectrum $\frac{1}{c\tau(\nu)}$ to be measured. Each data point in a cavity loss spectrum was the mean of up to 600 individual ring-down events, with outliers filtered by discarding ring-down times more than three standard deviations different to the data average.

The symmetry axis of the plasma effluent was defined as the z-axis and the optical axis of the cavity was defined as the y-axis. The axis perpendicular to the z- and y-axes was defined as the x-axis. A CAPJ was investigated by mounting it on two stepper motors (LNR502E/M, ThorLabs), such that the plasma effluent intersected the centre of the optical cavity. Two stepper motor controllers (BSC101, ThorLabs) moved the CAPJ in the (x,z)-plane to measure cavity loss spectra at different radial and axial positions in the effluent.

The best achievable spatial resolution of the optical cavity is estimated by the spot size of its lowest order transversal electromagnetic mode (TEM), typically referred to as TEM_{00}. The beam waist of the TEM_{00} in the centre of the cavity is given by

$$w_0 = \sqrt{\frac{L}{\pi\nu}}\left(\frac{1+g}{4(1-g)}\right)^{1/4}, \tag{1}$$

where L is the cavity length and $g = 1 - L/r$, the g-factor of the cavity mirrors with radius of curvature r. The beam waist w is defined as the distance from the beam centre at which its intensity is equal to I_0/e^2, where I_0 is the beam's intensity at its centre. For a Gaussian intensity profile, the beam waist is equal to the Gaussian width, i.e. $w = 2\cdot\sigma$. More details on this topic can be found in [46]. Using equation (1), the best achievable spatial resolution in the centre of the optical cavity is 2.76 mm (a $2.576\cdot\sigma$ interval, containing 99% of the total intensity). However, Klose *et al* determined the spatial resolution for the optical cavity used in this work to be 5.5mm [28]. This indicates that a higher order TEM was used for the measurements. In order to prevent any interference between the CAPJ nozzle and the cavity mode structure, no measurements were performed closer to the nozzle than $z = 3$ mm.

2.3. Data analysis procedure

The ring-down time of the laser light in the optical cavity depends on absorption by species along the optical path, in addition to loss mechanisms such as transmission through the cavity mirrors and scattering due to particulate matter (i.e. dust) or refractive index gradients [26]. Only effects due to optical absorption exhibit a strong dependence on the wavenumber of the laser. The cavity loss spectrum and absorption due to H_2O_2 can be related as follows:

$$\frac{1}{c\tau(\nu)} = \frac{A_{\text{int}}(\nu)}{L} + \frac{1}{c\tau_0(\nu)} \tag{2}$$

where c is the speed of light in a vacuum, $\tau(\nu)$ is the ring-down time measured at the wavenumber ν, $A_{\text{int}}(\nu)$ is the line-of-sight integrated absorbance of H_2O_2, L is the length of separation between the cavity mirrors, and $\tau_0(\nu)$ includes contributions to the ring-down time from the aforementioned cavity losses and the optical absorption of any other species present. The line-of-sight integrated absorbance can be defined as the density of H_2O_2 integrated along the line of sight multiplied by the sum of all overlapping broadened absorption lines at a given wavenumber, i.e.

$$A_{\text{int}}(\nu,x,z) = \int \alpha(\nu,x,y,z)\,\mathrm{d}y = n_{\text{int}}(x,z)\sum_t [S_t\cdot f(\nu,\nu_t)] \tag{3}$$

with

$$n_{\text{int}}(x,z) = \int n(x,y,z)\,\mathrm{d}y \quad \left[\frac{\text{molec.}}{\text{cm}^2}\right]. \tag{4}$$

Here, $\alpha(\nu)$ is the spectral absorption coefficient and n_{int} is the line-of-sight integrated density of H_2O_2. S_t is the line strength of transition t centred at wavenumber ν_t at 296 K, as the effluent of the CAPJs are almost at room temperature, with these two spectroscopic parameters provided by the HITRAN database [43–45, 47]. In this work, the measured transitions of H_2O_2 are expected to be in thermal equilibrium due to the high collision rates at atmospheric pressure. $f(\nu,\nu_t)$ is the line shape function of transition t at wavenumber ν. It is expected that Doppler broadening is negligible due to the relatively low temperatures typically observed in the effluents of both CAPJs [48, 49]. Given this, and the high collisionality at atmospheric pressure, it is assumed that the line shape function is largely dictated by pressure broadening and can therefore be described by a Lorentzian function

$$f(\nu,\nu_t) = \frac{1}{\pi}\frac{\gamma}{(\nu-\nu_t)^2+\gamma^2} \tag{5}$$

where γ is the pressure broadening coefficient and is discussed further in section 3.1.

In order to determine the line-of-sight integrated density n_{int} from the cavity loss spectrum, the following model was applied:

$$\frac{1}{c\tau(\nu)} = \frac{n_{\text{int}}}{\pi L}\sum_t\left[S_t\cdot\frac{\gamma}{(\nu-\nu_t)^2+\gamma^2}\right] + b_1\nu + b_0. \tag{6}$$

In this model, the assumption was made that the remaining contributions to the cavity losses besides the absorption of H_2O_2 can be approximated by a linear baseline, with baseline

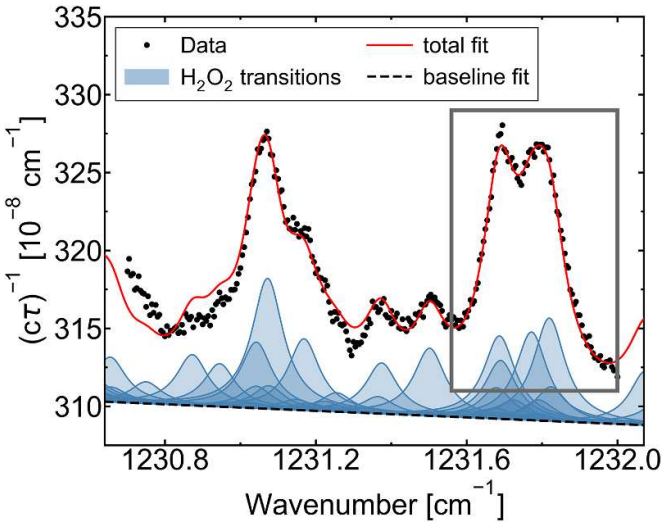

Figure 3. Model fit of a cavity loss spectrum measured in the effluent of the kINPen-sci plasma jet, including a linear baseline fit and contributions from individual H_2O_2 transitions. The grey box encompasses the spectral region of best fit chosen for the investigation of H_2O_2 in this work.

coefficients b_1 and b_0. A detailed discussion regarding this approximation is given in [28]. Using this model, a least-squares fitting routine is employed to obtain the line-of-sight integrated H_2O_2 density and baseline coefficients. This routine utilises the SciPy package for Python [50]. The spectra were fitted using 391 transitions of H_2O_2 between 1229 cm^{-1} and 1236 cm^{-1}, selecting transitions with a line strength higher than $10^{-23} cm^{-1}/(molec. \cdot cm^{-2})$. An example of a spectrum and applied fit are shown in figure 3. The fit is a close match to the data at the higher end of the wavenumbers measured. Towards lower wavenumbers the quality of the fit deteriorates. This is most likely due to the presence of a water absorption line centred at 1229.4 cm^{-1} skewing the shape of the absorption feature. While the line strength of the water absorption line is a factor of 10^3 lower than the more prominent H_2O_2 absorption lines, it is expected to significantly contribute to cavity loss due to the density of water contained in the effluent. Computational modelling of humidified helium CAPJs revealed that only about 3.8% of the H_2O admixture was dissociated in the plasma channel under comparable conditions to this study [33]. Furthermore, if it is assumed that the primary consumption pathway of H_2O in the plasma is through dissociation into OH and H, previous experimental measurements of OH taken shortly after the jet nozzle can be compared with the initial humidity concentration in the feed gas to yield approximate H_2O dissociation degrees of under 0.5% in the effluent [8, 24, 37]. These estimates pertain only to diffuse glow discharges due to the scarcity of OH measurements for relevant DBD-like CAPJs in humidified helium. However, due to their broadly similar plasma chemistries it is likely that the concentration of water in the effluent is close to the initial admixture concentration for both discharge types investigated in this work. Accordingly, the absorption feature within the spectral range 1231.57–1232.00 cm^{-1}, highlighted by the grey box, was selected for the investigation of H_2O_2 due to a better agreement with the model fit.

3. Results

3.1. Determination of the pressure broadening coefficient

In order to determine the line-of-sight integrated densities from the measured cavity loss spectra using equation (6), the pressure broadening coefficient, γ, must first be known. This parameter depends strongly on the temperature and gas composition of the effluent. Both of these parameters are expected to change with increasing distance from the nozzle, as the effluent gas mixes with the air and cools to the ambient temperature. The pressure broadening coefficient for H_2O_2 is only known for air and can therefore not be calculated independently. Using the established fitting model, treating the pressure broadening coefficient as an additional free-fit parameter allows it to be estimated, with only a selection of spectra with a good signal-to-noise ratio used to ensure reliable fitting. Figure 4 shows fitted spectra at different positions along the effluent for both CAPJs. The selected spectra are taken at positions within the Gaussian full width at half maximum of a radial distribution of line-of-sight-integrated H_2O_2 densities for a given axial position (see section 3.2).

In the case of the kINPen-sci plasma jet, the absorption feature is appreciably more broadened further away from the nozzle. In contrast, there is little difference in the shape of the two normalised COST-Jet spectra. It is evident that the pressure broadening coefficient differs between the two CAPJs. The highest signal-to-noise ratio is observed along the centre of the effluent, as the highest density of H_2O_2 is found in this region. Given that the measured signal diminishes along the effluent radius, attempting to fit spectra taken at larger radii with several free-fit parameters introduces an appreciable margin of error. Accordingly, variations of the pressure broadening coefficient as a function of radial position are not considered in this work. The assumption was made that the pressure broadening coefficient does not vary in the radial direction, allowing this parameter to be fixed radially and reducing the number of free-fit parameters in the model. The values of the pressure broadening coefficient along the effluent are obtained by taking the mean pressure broadening coefficient of a number of fitted spectra at each axial position, with all chosen spectra taken close to the effluent centre on the x-axis. The result of this is shown in figure 5, with lines indicating the trend added for ease of interpretation. For the kINPen-sci plasma jet, the pressure broadening coefficient increased with increasing distance from the nozzle, rising from 0.051 $cm^{-1}atm^{-1}$ at $z = 6$ mm to 0.079 $cm^{-1}atm^{-1}$ at $z = 33$ mm. Therefore, all spectra of the kINPen-sci plasma jet are processed with the pressure broadening coefficient fixed to the mean at the corresponding axial position. In contrast, no change in axial direction was observed within the margin of error for the COST-Jet. Spectra recorded for the COST-Jet also have a lower signal amplitude than those for the kINPen-sci plasma jet, increasing

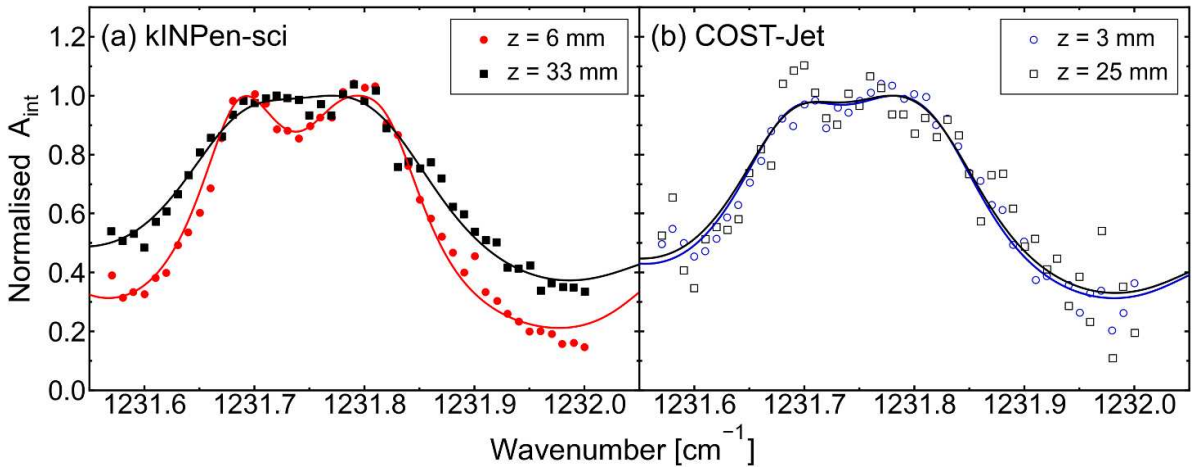

Figure 4. Relative change of the normalised line-integrated absorbance as a function of wavenumber. Fitted spectra are shown at different axial positions z for (a) the kINPen-sci plasma jet and (b) the COST-Jet.

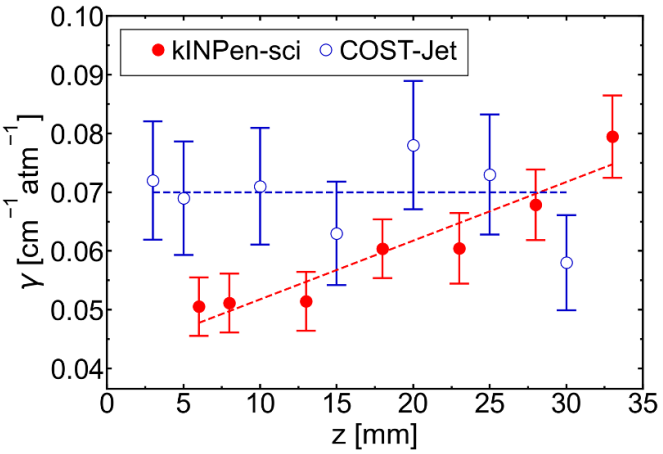

Figure 5. The obtained pressure broadening coefficient γ as a function of the axial position. Lines indicating a trend are included for the kINPen-sci plasma jet and for the COST-Jet.

the relative error margin. As such, there is not enough evidence to treat the pressure broadening coefficient independently for each axial position, and it is fixed for the COST-Jet spectra as 0.07 ± 0.01 cm^{-1}atm^{-1}. See section 4.3 for a discussion on the possible causes of the observed trends.

3.2. Determination of spatially resolved densities

In figures 6 and 7, the line-of sight integrated density of H_2O_2 is shown as a function of the radial distance x to the effluent's centre measured at different axial positions z for the COST-Jet and the kINPen-sci plasma jet, respectively. For any given axial position, the radial distribution of line-of-sight integrated H_2O_2 densities can be represented by a Gaussian function

$$n_{\mathrm{int}}(x) = n_0 w \sqrt{\frac{\pi}{2}} \cdot \exp\left[-2\frac{x^2}{w^2}\right]. \tag{7}$$

Here, n_0 is the density amplitude of H_2O_2 at the radial centre of the effluent, w is the Gaussian width, and the x-coordinate is normalised to the centre of the Gaussian to account for any minor axial tilt of the mounted CAPJ. Under the assumption that the effluent, and therefore the distribution of H_2O_2, is rotationally symmetric, an Abel inversion yields the following expression for the radial distribution of the absolute H_2O_2 number density

$$n(r) = n_0 \cdot \exp\left[-2\frac{r^2}{w^2}\right], \tag{8}$$

where $r = \sqrt{x^2 + y^2}$ defines the radial distance from the centre of the effluent in polar coordinates. It follows that n_0 and w can be extracted from Gaussian fits of the line-of-sight integrated density and substituted into equation (8) to obtain a continuous distribution of the density of H_2O_2 on the (x,y) plane. These fits are shown in figure 6 for the COST-Jet as blue curves and in figure 7 for the kINPen-sci plasma jet as red curves.

A detailed error analysis was performed to determine the error of each data point. This included the error of fitting the cavity loss spectra, the uncertainty of the pressure broadening coefficient and the uncertainty of the measurement method itself. Within the fitting procedure of the Gaussian functions, each data point was weighted based on their relative error. Consequently, data points with a lower relative error contribute more to the fit than data points with a higher relative error. Deviations from the Gaussian shape occur more prominently on the wings of the distribution. Some data points even have negative line-of-sight integrated densities as a result of fitting a cavity loss spectrum with a low signal-to-noise ratio. Those data points contribute very little to the fit and are intentionally not excluded from the data set, in order to transparently show the difficulties of measurements with this experimental setup. Moreover, an additional source of error in the determined H_2O_2 densities arises from the temperature uncertainty. Employing the HITRAN Application Programming

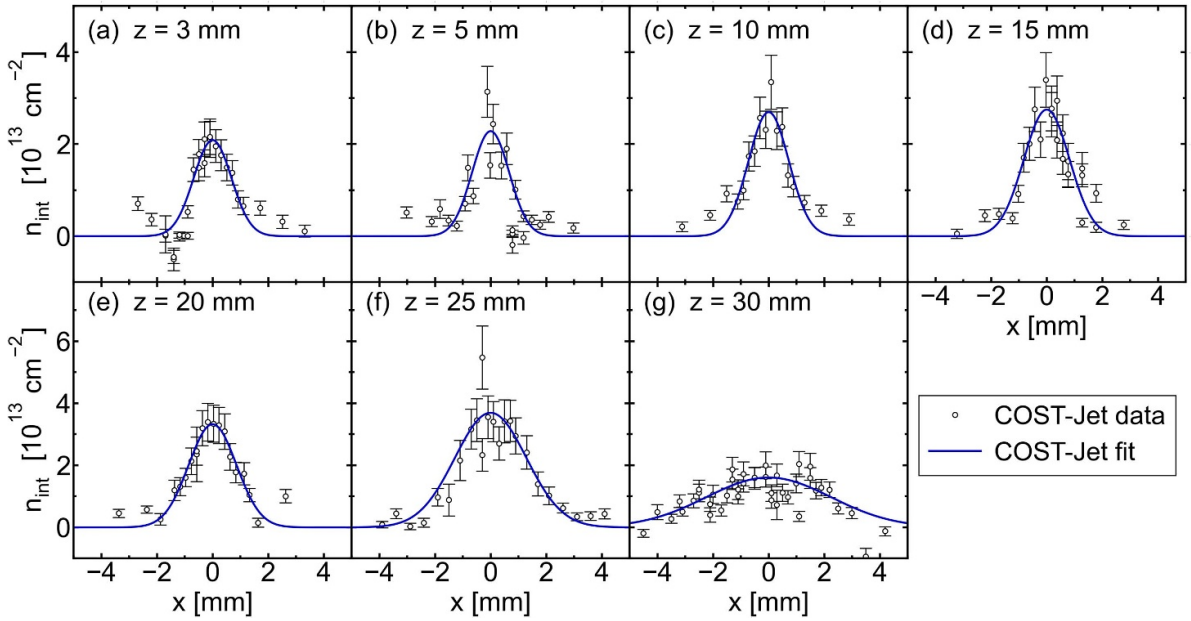

Figure 6. Measured radial distribution of the line-of-sight integrated H_2O_2 density at several positions along the effluent axis of the COST-Jet, together with applied Gaussian fits.

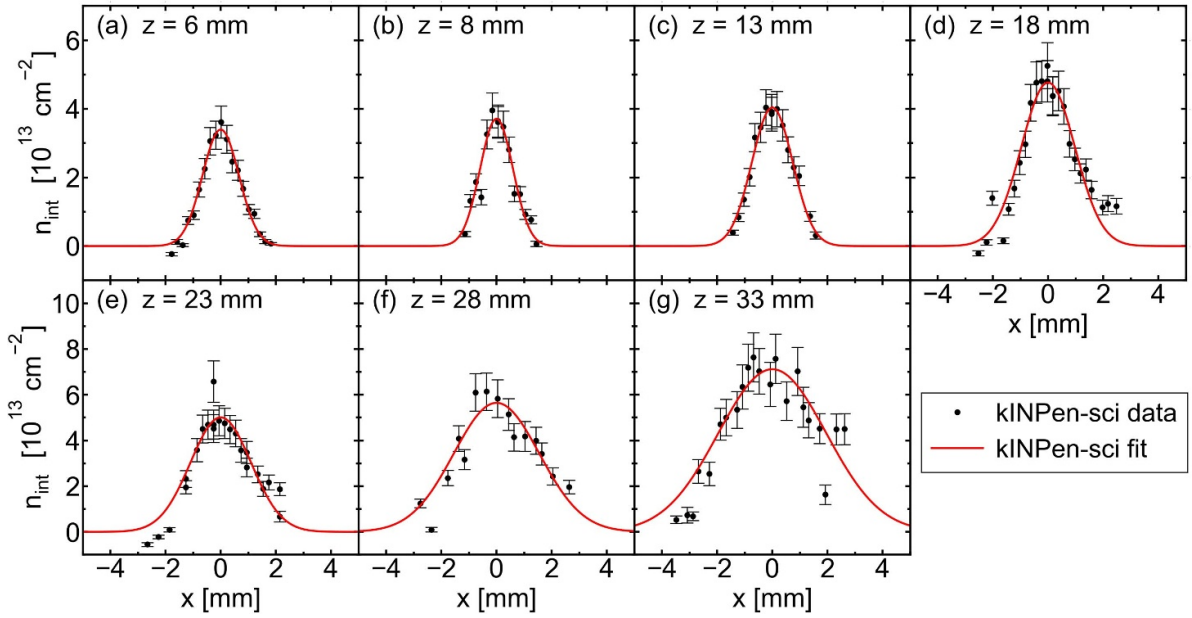

Figure 7. Measured radial distribution of the line-of-sight integrated H_2O_2 density at several axial positions along the effluent of the kINPen-sci plasma jet, together with applied Gaussian fits.

Interface (HAPI) [51], it was determined that an increase in gas temperature from 293 K to 320 K results in a 4% increase in the sum of line strengths used to fit the measured H_2O_2 spectra. This demonstrates that small temperature changes have a negligible effect on the H_2O_2 densities determined in this work.

Given that all radial profiles can be represented by a Gaussian function, determining n_0 and w for a range of axial positions allows these parameters to be fit with polynomial functions, thus characterising the behaviour of H_2O_2 along the effluent axis. Polynomials of the form

$$f(z) = a \cdot z^b + c \tag{9}$$

are used, where $f(z)$ is the density amplitude n_0 or the Gaussian width w as a function of axial position, b is the integer polynomial order, and a and c are fitted coefficients. In figures 8(a) and (b), the density amplitude and the Gaussian width are shown as a function of axial position, respectively. Both parameters are found to be described best by fifth order polynomials for the COST-Jet, while for the kINPen-sci plasma jet they are best described by second order polynomials. Notably,

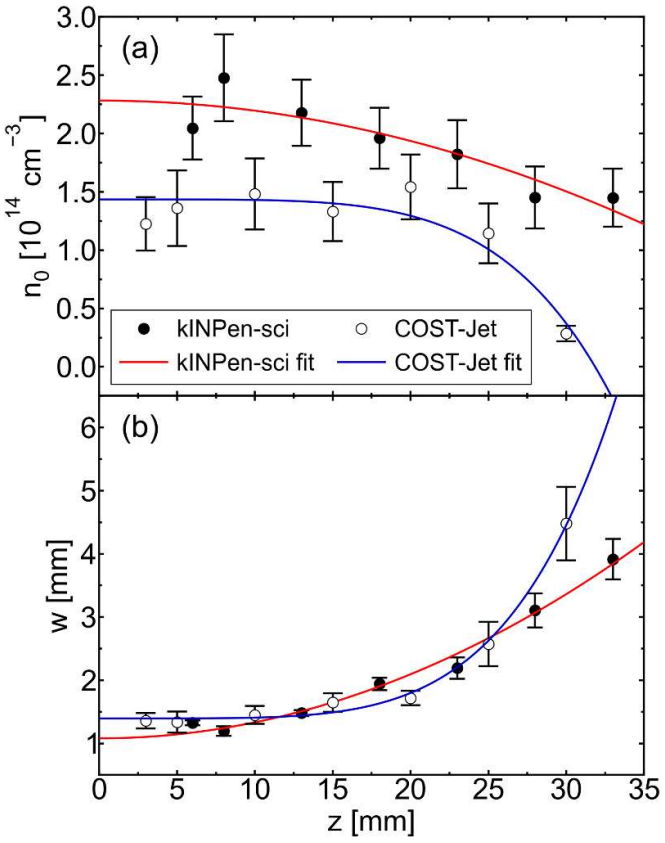

Figure 8. (a) The density amplitude n_0 as a function of axial position, and (b) the Gaussian width w as a function of axial position. $z = 0$ is the tip of the jet nozzle. Both parameters are best described by a fifth order polynomial for the COST-Jet, and by a second order polynomial for the kINPen-sci plasma jet.

there appears to be a slight initial increase in H_2O_2 density amplitude along the z-axis for both jets, based on the closest data points to the nozzle in figure 8(a).

Substituting the polynomial functions into equation (8) interpolates between the experimental data, yielding a continuous, spatially resolved density distribution of H_2O_2. In figure 9, cross-sections of the H_2O_2 distribution on the $y = 0$ plane for both CAPJs are shown. The maximum H_2O_2 density in the effluent of the COST-Jet is 1.4×10^{14} cm^{-3}, measured at $z = 3$ mm at the radial centre. At the same axial position, Willems *et al* measured a similar H_2O_2 density of around 1.2×10^{14} cm^{-3} for a COST-Jet supplied with a helium feed gas with roughly 2800 ppm H_2O [37]. The peak in figure 9(a) remains largely constant up to $z = 15$ mm, with a decay of a factor of 3.5 in H_2O_2 density from $z = 15$ mm to $z = 30$ mm. The radial distribution of the H_2O_2 density is about 4 mm between $z = 3$ mm and $z = 15$ mm, widening past this to a maximum value of around 12 mm at $z = 30$ mm. The maximum density in the effluent of the kINPen-sci plasma jet is 2.3×10^{14} cm^{-3}, found at the closest measured position to the nozzle, $z = 6$ mm and $x = 0$ mm. The density through the centre of the effluent remains high over the range measured, dropping by a factor of 1.6 by $z = 33$ mm. The radial distribution of the H_2O_2 density is around 4 mm close to the nozzle, increasing to a width of about 10 mm by $z = 33$ mm. From the error analysis procedure, the upper limit for the error of the H_2O_2 density was determined to be $\pm16\%$ for the COST-Jet and $\pm12\%$ for the kINPen-sci plasma jet.

4. Discussion

4.1. Discussion of the distinct spatial distribution of H_2O_2 for both CAPJs

The spatial distribution of H_2O_2 in the effluent of the COST-Jet suggests minimal mixing of H_2O_2 with the ambient air up to $z = 15$ mm. At $z = 15 - 20$ mm, the H_2O_2 starts to diffuse into the surrounding air, with the density dropping sharply past this point. This is reflected in the fit of the COST-Jet's density amplitude and the associated Gaussian width, shown as a function of axial position in figures 8(a) and (b), respectively. Both parameters are largely constant for the first 15 mm from the nozzle, with the Gaussian width increasing sharply at further distances and the density amplitude at the centre of the effluent decreasing in turn. For the kINPen-sci plasma jet, the H_2O_2 distribution starts expanding radially much closer to the jet nozzle. However, the mixing of H_2O_2 with the surrounding air is much more gradual further into the effluent, with around 60% of the maximum density still present in the effluent core at the limit of the range measured. H_2O_2 was measured up to 33 mm from the nozzle of the kINPen-sci plasma jet without having reached the detection limit, while the detection limit was reached at $z = 30$ mm for the COST-Jet.

The difference in the distinct spatial distribution of H_2O_2 in the effluent of both CAPJs is evident in the different polynomial functions best describing their associated Gaussian width and their density amplitude as a function of the axial coordinate. For the kINPen-sci plasma jet both parameters are best described by a steady second order polynomial, while for the COST-Jet a comparably steep fifth order polynomial fits best.

The distribution of H_2O_2 close to the nozzle of the kINPen-sci plasma jet may be a result of its electrode arrangement. The electrode pin positioned in the centre of the capillary may obstruct the feed gas flow, creating a volatile flow pattern that causes the H_2O_2 to mix more readily with the ambient air 4 mm after the nozzle [49]. Contrary to this, the COST-Jet's plasma channel is 30 mm long and unobstructed [48]. This likely forces heavy species into a highly consistent flow pattern by the time they exit the nozzle, resulting in less initial mixing with the ambient air.

4.2. Influence of the discharge type on the chemical pathways of H_2O_2

On average, the H_2O_2 densities measured for the kINPen-sci plasma jet are roughly a factor of 2 higher than those measured for the COST-Jet. It is known that the density of H_2O_2 generated by atmospheric pressure plasmas is correlated with the plasma dissipated power [52–54]. Based on the COST-Jet specifications, the conditions used in this work are estimated to

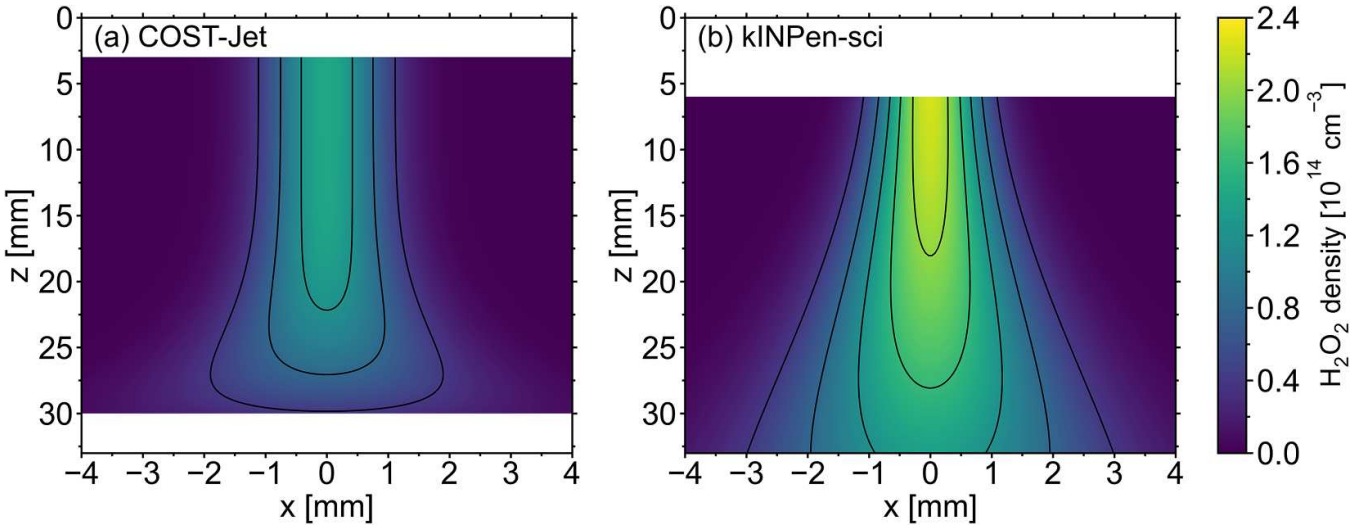

Figure 9. Density distribution of H_2O_2 in the effluent region of (a) the COST-Jet and (b) the kINPen-sci plasma jet. $y = 0$ in both cases. The effluent protrudes freely into open air.

supply roughly 1 W of power to the plasma [39]. The kINPen-sci plasma jet is also expected to supply approximately 1 W of power to the plasma [31]. However, for the COST-Jet the power is expected to be deposited over the full length of the electrodes, while for the kINPen-sci plasma jet the electrode arrangement allows the power to be deposited in a more localised volume, which results in a higher energy density. It was not possible to experimentally match the power deposited into both plasmas beyond these estimates. As such, it is possible that a mismatch in coupled power may contribute to the different densities observed between the two CAPJs. A study of this contribution remains for future investigations.

Furthermore, the discharge physics might also be different for the two CAPJs [55]. The COST-Jet is a capacitively coupled non-thermal plasma source that produces, under the operational conditions of this study, a diffuse glow discharge distributed homogeneously between the two electrodes. It is assumed that the electric fields mostly confine the electrons to the plasma channel, as evidenced by photon emission not extending past the electrode housing. On the other hand, the kINPen-sci plasma jet is a DBD-like, non-thermal plasma source, which shows filamentary behaviour when operated with argon as well as in helium [56]. The high electric fields of such filaments are expected to stimulate the production of higher densities of hot electrons than found in the diffuse plasma bulk of the COST-Jet, and in a more localised volume. These hot electrons can readily dissociate the water admixture

$$e^- + H_2O \rightarrow OH + H + e^-, \qquad (R1)$$

and the hydroxyl radicals produced through this dissociation can form H_2O_2 in a three-body reaction with the helium available in the feed gas

$$OH + OH + He \rightarrow H_2O_2 + He, \qquad (R2)$$

resulting in a higher formation of H_2O_2. It can be concluded that the higher H_2O_2 densities observed in the effluent of the kINPen-sci plasma jet are a result of a greater fraction of water admixture being dissociated when compared to the COST-Jet, which consequently results in a different chemical composition of the effluent between the two CAPJs.

The presented spatial distributions can also be used to infer where H_2O_2 formation occurs. For both CAPJs their maximum H_2O_2 density was determined in the effluent core at the closest axial position to the nozzle measured, with the density dropping with increasing distance from the nozzle. It can be concluded that most H_2O_2 formation occurs either within, or shortly after, the plasma channel. This observation is in agreement with the reaction chemistry presented in [16], in which it is expected that the bulk of H_2O_2 is produced in the active plasma region, via the chain of reactions (R1) and (R2). Beyond the active plasma region, free electrons rapidly recombine with heavy particles. Based on visible photon emission, in this work the electron density is estimated to diminish to background levels by $z = 7.5$ mm for the kINPen-sci plasma jet and by the nozzle exit for the COST-Jet. Beyond these positions, the lack of electrons and short effective lifetime of OH results in an exponential decay in OH density. Previous studies reported a decrease in OH density by a factor of five in the first 5–10 mm after the active plasma region depending on the feed gas humidity [8, 24]. The net production of H_2O_2 in the far effluent via this pathway is therefore expected to be negligible. This is further reinforced by findings from Gorbanev *et al*, who treated an aqueous sample with a COST-Jet supplied with humidified helium [57]. Combining experiment and computational modelling, they determined that the H_2O_2 concentration in the treated liquid was largely unaffected by the ambient humidity in the effluent or the distance between the COST-Jet and the sample. From this, they concluded that the H_2O_2 measured in the liquid was predominantly formed within the plasma channel. Willems *et al* made a similar observation, measuring a H_2O_2 density distribution along the effluent of a COST-Jet analogue that peaked at around $z = 2$ mm and gradually decreased with axial position [37]. They compared this to

a computational model in the same study and suggested that the trend is due to the radial diffusion losses of H_2O_2 outstripping the availability of OH with distance from the nozzle.

4.3. Discussion of the pressure broadening coefficient

The pressure broadening coefficient as a function of the axial position, as shown in figure 5, is markedly different between the COST-Jet and the kINPen-sci plasma jet. For the first 28 mm of the effluent, the pressure broadening coefficient for the COST-Jet is consistently higher than those determined for the kINPen-sci plasma jet. As the kINPen-sci plasma jet is, due to its DBD-like discharge type, more efficient in dissociating H_2O, the higher amount of water present in the effluent of the COST-Jet may lead to higher pressure broadening of the absorption lines of H_2O_2.

The increase in the broadening coefficient along the effluent of the kINPen-sci plasma jet is likely due to mixing with the ambient air. Helium has a lower relative mass than nitrogen and oxygen, and should exert a lower degree of pressure broadening as a result. If the effluent of the kINPen-sci plasma jet is initially relatively pure and is progressively diluted by mixing with ambient air along its axis, the change in gas composition may lead the pressure broadening coefficient to increase with increasing distance from the nozzle. In addition, a larger pressure broadening coefficient was found for the kINPen-sci plasma jet operated with humidified argon as a feed gas, suggesting an effect of the atomic or molecular mass of the feed gas of choice [28].

Moreover, possible temperature gradients, stemming from equalisation of the gas temperature in the effluent to room temperature, may also contribute to the trend in the pressure broadening coefficient observed for the kINPen-sci plasma jet. It remains for future investigations to elucidate why the same linear increase would not then be observed along the effluent axis of the COST-Jet, and whether this is due to the differences in the chemical composition of the effluent or simply the result of an overall lower absorption signal due to the on average lower densities of H_2O_2.

4.4. A comparison of argon and helium as a feed gas for the kINPen-sci plasma jet

First insights into the impact of the chosen primary feed gas on the H_2O_2 density distribution can be obtained by comparing the spatial distribution of H_2O_2 in the effluent of the kINPen-sci plasma jet in figure 9(b) with the spatial distribution of H_2O_2 in the effluent of the same jet supplied with humidified argon as a feed gas, reported by Klose *et al* [28]. The argon mixture is introduced at a flow rate of 3 slm compared to 1 slm in the helium case. This accounts for helium having a higher thermal conductivity than argon, as lower flow rates (and therefore increased residence times) may be more ideal for sustaining the plasma chemistry of helium mixtures [58]. The radial distribution of the H_2O_2 density in the first 10 mm of the effluent is larger for the reported argon case than for the present helium case. At $z = 10$ mm, the H_2O_2 is distributed across a diameter of 4 mm in helium, whereas in argon it is present in appreciable densities across a diameter of roughly 6 mm. This is likely due to the difference in carrier gas density. Argon is ten times heavier then helium and should therefore undergo more vigorous mixing with the surrounding air due to its higher momentum, especially when coupled with the higher flow rate used in the argon case.

The feed gas humidity reported in the argon case is 1600 ppm, while (3300 $\pm$ 100) ppm is used in the present helium study. It has been shown that the production of H_2O_2 scales strongly with increasing humidity for low feed gas concentrations, before gradually saturating above 4000 ppm H_2O [37, 52, 57]. Given this scaling, an appreciably lower H_2O_2 density may be expected for the argon case due to the 50% lower H_2O concentration. However, the magnitude of absolute H_2O_2 densities is notably similar between the carrier gases. The maximum density of H_2O_2 is 2.3×10^{14} cm^{-3} for the helium-dominated feed gas, while a maximum density of approximately 2.0×10^{14} cm^{-3} is reported for the argon-dominated mixture [28]. As these values cannot be distinguished within the bounds of experimental uncertainty, this indicates that the choice of carrier gas plays an important role in determining the production of H_2O_2 by CAPJs. Numerous studies comparing the discharge properties of argon and helium plasmas at atmospheric pressure have shown that argon plasmas typically possess higher electron densities than helium plasmas, while helium plasmas are sustained with a higher electron temperature than in argon [59–63]. This has been attributed to helium having a higher first ionisation energy and first excitation energy than argon [63]. As discussed in section 4.2, the electron impact dissociation of H_2O into OH and H is expected to scale with electron density, in turn determining the production of H_2O_2 through OH recombination in reaction (R2). This is supported by measurements from Du *et al* in a comparative study of OH densities in helium and argon plasmas [64]. The density of OH was found to be roughly three times higher in argon than in helium for a feed gas humidity comparable to the present work. Hence, it can be posited that the greater electron density of argon plasmas is partly responsible for the near equal peak H_2O_2 densities measured in the effluent of the kINPen-sci plasma jet when operated with humidified argon or humidified helium, despite the H_2O concentration being 50% lower in the argon case [28].

5. Conclusion

CAPJs are efficient sources of H_2O_2, a RONS key to the application of plasmas in biomedicine. Different RONS vary in how they are distributed throughout the plasma effluent, with these distributions affected by a species' mass, available reaction pathways and also the CAPJ's discharge type. As such, the mixture and dosage of species received by a substrate is strongly dependent on its position relative to the plasma source. Significant work has previously been undertaken to measure the spatial distributions of RONS in the effluent of humidified argon plasmas, although the same information is currently scarce for humidified helium plasmas.

In this study, the spatial distribution of H_2O_2 is obtained for the effluent region of a COST-Jet and kINPen-sci plasma jet supplied with humidified helium as a feed gas. The measurements are performed using continuous wave CRDS, with a feature in the ν_6 absorption band of H_2O_2 probed within the spectral range of 1231.57–1232.00 cm^{-1} to obtain its line-of-sight integrated density at different positions in the effluent. Absolute number densities of H_2O_2 are obtained by performing an Abel inversion on the radial distribution of line-of-sight integrated densities. Polynomial fits for the density amplitude as well as for the Gaussian width are used to obtain a continuous, spatially resolved distribution of H_2O_2 for both CAPJs.

The H_2O_2 distribution close to the COST-Jet nozzle appears to undergo minimal mixing with the ambient air when compared with the density distribution of H_2O_2 for the kINPen-sci plasma jet, although this mixing occurs very rapidly at more than 15 mm into the effluent of the COST-Jet. For the kINPen-sci plasma jet, the H_2O_2 has a wider radial distribution close to the nozzle, but the distribution widens more gradually further into the effluent than in case of the COST-Jet. These observations may stem from the electrode arrangement affecting the flow properties of the effluent. It is also noted that the majority of H_2O_2 production occurs within, or up to a few millimetres after, the plasma channel. The maximum H_2O_2 densities determined in the effluent of the COST-Jet and kINPen-sci plasma jet are 1.4×10^{14} cm^{-3} and 2.3×10^{14} cm^{-3}, respectively. The average density of H_2O_2 in the effluent of the kINPen-sci plasma jet is roughly twice as large as determined for the COST-Jet. There is evidence that the higher H_2O_2 densities observed in the effluent of the kINPen-sci are a result of a greater fraction of water being dissociated when compared to the COST-Jet, although a mismatch in deposited power cannot be excluded. Near-equivalent densities of H_2O_2 are observed for the kINPen-sci plasma jet and a similar work that utilises argon as a feed gas instead of helium, despite a factor of 2 difference in humidity concentration.

This work serves to highlight the difference of the distinct spatial distribution of H_2O_2 in the effluent of both types of plasma jets when considering their direct application in biomedicine.

Data availability statement

The data that support the findings of this study are openly available at the following URL/DOI: https://doi.org/10.34 711/inptdat.784.

Acknowledgments

The authors wish to thank Philipp Mattern and Ronny Brandenburg for many fruitful discussions. This work was partly funded by INP internal funding. The authors also gratefully acknowledge financial support from the UK EPSRC (EP/S026584/1 & EP/S025790/1) and the Norma Ann Christie Scholarship.

ORCID iDs

B Harris https://orcid.org/0000-0002-4036-8585
L Krös https://orcid.org/0009-0001-1129-8063
A S C Nave https://orcid.org/0000-0003-4131-7576
E Wagenaars https://orcid.org/0000-0002-5493-3434
J H van Helden https://orcid.org/0000-0001-8925-2607

References

[1] Graves D B 2012 *J. Phys. D: Appl. Phys.* **45** 263001
[2] Shaw D, West A, Bredin J and Wagenaars E 2016 *Plasma Sources Sci. Technol.* **25** 065018
[3] Brandenburg R *et al* 2019 *Plasma Process. Polym.* **16** 1700238
[4] Brisset A, Gibson A R, Schröter S, Niemi K, Booth J P, Gans T, O'Connell D and Wagenaars E 2021 *J. Phys. D: Appl. Phys.* **54** 285201
[5] Klose S J, Ellis J, Riedel F, Schröter S, Niemi K, Semenov I L, Weltmann K D, Gans T, O'Connell D and van Helden J H 2020 *Plasma Sources Sci. Technol.* **29** 125018
[6] Dedrick J, Schröter S, Niemi K, Wijaikhum A, Wagenaars E, de Oliveira N, Nahon L, Booth J P, O'Connell D and Gans T 2017 *J. Phys. D: Appl. Phys.* **50** 455204
[7] West A, van der Schans M, Xu C, Cooke M and Wagenaars E 2016 *Plasma Sources Sci. Technol.* **25** 02LT01
[8] Schröter S *et al* 2018 *Phys. Chem. Chem. Phys.* **20** 24263
[9] Brisset A, Harris B, Dickenson A, Niemi K, Walsh J and Wagenaars E 2022 *Plasma Sources Sci. Technol.* **31** 045008
[10] Verreycken T, Van der Horst R M, Baede A H F M, Van Veldhuizen E M and Bruggeman P J 2012 *J. Phys. D: Appl. Phys.* **45** 045205
[11] Niedźwiedź I, Waśko A, Pawłat J and Polak-Berecka M 2019 *Pol. J. Microbiol.* **68** 153–64
[12] Zimu X *et al* 2020 *Plasma Sci. Technol.* **22** 103001
[13] Dubey S K, Parab S, Alexander A, Agrawal M, Achalla V P K, Pal U N, Pandey M M and Kesharwani P 2022 *Process Biochem.* **112** 112–23
[14] Reuter S, Sousa J S, Stancu G D and van Helden J H 2015 *Plasma Sources Sci. Technol.* **24** 054001
[15] Winter J *et al* 2014 *J. Phys. D: Appl. Phys.* **47** 285401
[16] Reuter S, Winter J, Iséni S, Schmidt-Bleker A, Dünnbier M, Masur K, Wende K and Weltmann K D 2014 *IEEE Trans. Plasma Sci.* **43** 3185–92
[17] O'Keefe A and Deacon D A 1988 *Rev. Sci. Instrum.* **59** 2544–51
[18] Lang N, Macherius U, Wiese M, Zimmermann H, Röpcke J and van Helden J H 2016 *Opt. Express* **24** A536–43
[19] Wang C and Srivastava N 2010 *Eur. Phys. J.* D **60** 465–77
[20] Srivastava N and Wang C 2011 *IEEE Trans. Plasma Sci.* **39** 918–24
[21] Srivastava N and Wang C 2011 *J. Appl. Phys.* **110** 053304
[22] Wang C and Wu W 2013 *J. Phys. D: Appl. Phys.* **46** 464008
[23] Zaplotnik R, Bišćan M, Krstulović N, Popović D and Milošević S 2015 *Plasma Sources Sci. Technol.* **24** 054004
[24] Benedikt J, Schröder D, Schneider S, Willems G, Pajdarová A, Vlček J and Schulz-Von Der Gathen V 2016 *Plasma Sources Sci. Technol.* **25** 045013
[25] Gianella M, Reuter S, Aguila A L, Ritchie G A D and van Helden J H 2016 *New J. Phys.* **18** 113027
[26] Gianella M, Reuter S, Press S A, Schmidt-Bleker A, van Helden J H and Ritchie G A D 2018 *Plasma Sources Sci. Technol.* **27** 095013
[27] Klose S J, Manfred K M, Norman H C, Ritchie G A D and van Helden J H 2020 *Plasma Sources Sci. Technol.* **29** 085011

[28] Klose S J, Kroes L and van Helden J H 2023 *Front. Phys.* **11** 1221181
[29] Verreycken T, Mensink R, Van Der Horst R, Sadeghi N and Bruggeman P J 2013 *Plasma Sources Sci. Technol.* **22** 055014
[30] Yatom S, Luo Y, Xiong Q and Bruggeman P J 2017 *J. Phys. D: Appl. Phys.* **50** 415204
[31] Reuter S, von Woedtke T and Weltmann K D 2018 *J. Phys. D: Appl. Phys.* **51** 233001
[32] Klose S J, Bansemer R, Brandenburg R and van Helden J H 2021 *J. Appl. Phys.* **129** 063304
[33] Schröter S, Bredin J, Gibson A R, West A, Dedrick J P, Wagenaars E, Niemi K, Gans T and O'Connell D 2020 *Plasma Sources Sci. Technol.* **29** 105001
[34] Myers B, Barnat E and Stapelmann K 2021 *J. Phys. D: Appl. Phys.* **54** 455202
[35] Stapelmann K, Myers B, Quesada M H, Lenker E and Ranieri P J 2021 *J. Phys. D: Appl. Phys.* **54** 434003
[36] van den Bekerom D, Tahiyat M M, Huang E, Frank J H and Farouk T I 2023 *Plasma Sources Sci. Technol.* **32** 015006
[37] Willems G, Benedikt J and Von Keudell A 2017 *J. Phys. D: Appl. Phys.* **50** 335204
[38] Preissing P, Korolov I, Schulze J, Schulz-von der Gathen V and Boeke M 2020 *Plasma Sources Sci. Technol.* **29** 125001
[39] Golda J *et al* 2016 *J. Phys. D: Appl. Phys.* **49** 084003
[40] Gorbanev Y, Golda J, Schulz-von der Gathen V and Bogaerts A 2019 *Plasma* **2** 316–27
[41] Bekeschus S, Schmidt A, Weltmann K D and von Woedtke T 2016 *Clin. Plasma Med.* **4** 19–28
[42] Dünnbier M, Schmidt-Bleker A, Winter J, Wolfram M, Hippler R, Weltmann K D and Reuter S 2013 *J. Phys. D: Appl. Phys.* **46** 435203
[43] Perrin A, Valentin A, Flaud J, Camypeyret C, Schriver L, Schriver A and Arcas P 1995 *J. Mol. Spectrosc.* **171** 358–73
[44] Perrin A, Flaud J M, Camy-Peyret C, Schermaul R, Winnewisser M, Mandin J Y, Dana V, Badaoui M and Koput J 1996 *J. Mol. Spectrosc.* **176** 287–96
[45] Klee S, Winnewisser M, Perrin A and Flaud J M 1999 *J. Mol. Spectrosc.* **195** 154–61
[46] Berden G and Engeln R 2009 *Cavity Ring-Down Spectroscopy: Techniques and Applications* (Wiley)
[47] Gordon I E *et al* 2022 *J. Quant. Spectrosc. Radiat. Transfer* **277** 107949
[48] Kelly S, Golda J, Turner M M and Schulz-von der Gathen V 2015 *J. Phys. D: Appl. Phys.* **48** 444002
[49] Schmidt-Bleker A, Reuter S and Weltmann K D 2015 *J. Phys. D: Appl. Phys.* **48** 175202
[50] Virtanen P *et al* 2020 *Nat. Methods* **17** 261–72
[51] Kochanov R V, Gordon I, Rothman L, Wcisło P, Hill C and Wilzewski J 2016 *J. Quant. Spectrosc. Radiat. Transfer* **177** 15–30
[52] Vasko C A, Liu D X, van Veldhuizen E M, Iza F and Bruggeman P J 2014 *Plasma Chem. Plasma Process.* **34** 1081–99
[53] Yayci A, Dirks T, Kogelheide F, Alcalde M, Hollmann F, Awakowicz P and Bandow J E 2020 *ChemCatChem* **12** 5893–7
[54] Schüttler S, Jolmes L, Jeß E, Tschulik K and Golda J 2023 *Plasma Process. Polym.* e2300079
[55] Brandenburg R 2017 *Plasma Sources Sci. Technol.* **26** 053001
[56] Schmidt-Bleker A, Norberg S A, Winter J, Johnsen E, Reuter S, Weltmann K D and Kushner M J 2015 *Plasma Sources Sci. Technol.* **24** 035022
[57] Gorbanev Y, Verlackt C, Tinck S, Tuenter E, Foubert K, Cos P and Bogaerts A 2018 *Phys. Chem. Chem. Phys.* **20** 2797–808
[58] Murphy A B 1997 *IEEE Trans. Plasma Sci.* **25** 809–14
[59] Jonkers J, Van De Sande M, Sola A, Gamero A and Van Der Mullen J 2002 *Plasma Sources Sci. Technol.* **12** 30
[60] Moravej M, Yang X, Nowling G, Chang J, Hicks R and Babayan S 2004 *J. Appl. Phys.* **96** 7011–7
[61] Benedikt J, Raballand V, Yanguas-Gil A, Focke K and Von Keudell A 2007 *Plasma Phys. Control. Fusion* **49** B419
[62] Hofmann S, Van Gessel A, Verreycken T and Bruggeman P 2011 *Plasma Sources Sci. Technol.* **20** 065010
[63] Golda J, Held J and Schulz-von der Gathen V 2020 *Plasma Sources Sci. Technol.* **29** 025014
[64] Du Y, Nayak G, Oinuma G, Peng Z and Bruggeman P J 2017 *J. Phys. D: Appl. Phys.* **50** 145201